Chemical vapor deposition of a single crystalline MoS_2 monolayer through anisotropic 2D crystal growth on stepped sapphire surface

*Iryna Kandybka[1,2], Benjamin Groven[1], Henry Medina Silva[1], Stefanie Sergeant[1], Ankit Nalin Mehta[1], Serkan Koylan[1,3], Yuanyuan Shi[1,▲], Sreetama Banerjee[1], Pierre Morin[1], Annelies Delabie[1,2]**

[1]imec, Kapeldreef 75, Leuven, 3001, Belgium

[2]Department of Chemistry KU Leuven, Celestijnenlaan 200F, Leuven, 3001, Belgium

[3]Quantum Solid State Physics KU Leuven, Celestijnenlaan 200D, Leuven, 3001, Belgium

E-mail: Annelies.delabie@imec.be; iryna.kandybka@imec.be

ABSTRACT

Recently, a step-flow growth mode has been proposed to break the inherent molybdenum disulfide (MoS_2) crystal domain bimodality and yield single crystalline MoS_2 monolayer on commonly employed sapphire substrates. This work reveals an alternative growth mechanism during metal-organic chemical vapor deposition (MOCVD) of a single crystalline MoS_2 monolayer through anisotropic 2D crystal growth. During early growth stages, the epitaxial symmetry and commensurability of sapphire terraces rather than the sapphire step inclination ultimately govern the MoS_2 crystal orientation. Strikingly, as the MoS_2 crystals continue to grow laterally, the sapphire steps transform the MoS_2 crystal geometry into diamond-shaped domains presumably by anisotropic diffusion of ad-species and facet development. Even though these MoS_2 domains nucleate on sapphire with predominantly a bimodal 0^o and 60^o azimuthal rotation, the individual domains reach lateral dimensions up to 200 nm before merging seamlessly into a single crystalline MoS_2 monolayer upon coalescence. Plan-view Transmission Electron Microscopy reveals the single crystalline nature across 50 µm by 50 µm inspection areas. As a result, the median carrier mobility of MoS_2 monolayers peaks at 25 $cm^2 V^{-1} s^{-1}$ with the highest value reaching 28 $cm^2 V^{-1} s^{-1}$. This work details synthesis-structure correlations and the possibilities to tune the structure and material properties through substrate topography towards various applications in nanoelectronics, catalysis and nanotechnology. Moreover, shape modulation through anisotropic growth phenomena on stepped surfaces can provide opportunities for nanopatterning for a wide range of materials.

KEYWORDS: two-dimensional (2D) materials, nanoelectronics, chemical vapor deposition, transition metal dichalcogenides, van der Waals epitaxy, sapphire template, molybdenum disulfide

Two-dimensional (*2D*) materials have gathered widespread interest over the last decade because of their distinctive and versatile properties.[1–5] Successful proof of concepts for their implementation have been demonstrated in various fields, including electronics, optoelectronics, photonics, sensors, and memory devices. [6–9] Among the 2D materials, the semiconducting transition metal dichalcogenides (*TMDs*) received significant attention owing to their tunable bandgap, excellent electronic and optical properties, which are highly promising for the future application in nanoelectronic devices. [10–12] The semiconducting 2D TMD materials MoS_2 and WS_2 are channel materials of high potential for implementation in ultimately scaled electronic devices because of their atomic scale thickness. Moreover, the surface of ideal 2D crystals lacks dangling bonds. This can be highly beneficial for use as a channel material because defects at or near the semiconductor interface typically act as charge traps and scattering centers that inhibit charge transport. In addition, precise electrostatic gate control is possible in such 2D TMD channels because of their ultrathin body thickness and the low leakage current at the off state.[13] Indeed, nanoscale field-effect transistors with monolayer TMD channels have demonstrated a high charge carrier mobility of 200 $cm^2 V^{-1} s^{-1}$ and a large on/off current ratio of 10^6 - 10^8.[14]

Chemical vapor deposition (*CVD*) is currently the preferred deposition technique to produce large-area 2D materials for application in nano-electronic devices. Recent research efforts were dedicated to develop a deposition scheme for 2D TMDs that provides crystals with a controlled and reproducible crystallinity, structure, number of monolayers and properties across large area substrates.[15–18] Among those, approaching a single crystalline structure of 2D material is of prime importance, as grain boundaries and defects in the 2D crystals degrade the mobility of the semiconductor due to scattering of carriers.[19,20] In principle, the crystallographic orientation of a TMD monolayer can be controlled during epitaxial growth by translating crystal symmetry of the substrate on the deposited material. Epitaxial growth of a monocrystalline 2D material

by CVD requires a monocrystalline substrate or template. Ideally, because of the lack of out-of-plane chemical bonding, the template and the 2D layer adhere via van der Waals forces. This growth mechanism is different from the conventional epitaxy because of the absence of strong covalent bonding resulting in the relaxation of strict lattice-match conditions and is called van der Waals epitaxy.[21,22]

The challenge for epitaxial growth of 2D TMDs lies in understanding how to overcome the limitations imposed by the crystal symmetry of the template. Substrates such as (0001) sapphire (α-Al_2O_3) and (0001) AlN have been investigated for van der Waals epitaxy as a consequence of their hexagonal symmetry, wafer-size, availability, good thermal and chemical stability.[23] Literature predicts similar formation energy of TMD crystal domains oriented along the same direction (0°) and the opposite direction (±60°), hence domains can exist in two orientations.[24,25] Coalescence of domains oriented in the same direction may form large single-oriented regions. On the other hand, coalescence of domains of opposite orientation, so-called antiphase, inversion, or 60° rotated domains (twins), may introduce an antiphase boundary. Currently there is no consensus in the literature concerning the effect of antiphase boundaries on the electrical properties of the TMD monolayer, as some researchers suggest no impact on electrical performance,[24,26] whereas others demonstrate the degradation of the material electrical performance if the channel is built on the grain boundary.[27]

One proposed solution to break TMD domains' bimodality promotes a *step-flow growth mode*,[28–33] also dubbed *step-edge guided nucleation* in the earlier work.[34] Caused by a small and unintentional miscut from sapphire's principal hexagonal axis during the wafer fabrication process, a step- and terrace-like surface structure is characteristic for vicinal surfaces. The step electronic structure differs from the sapphire terraces, introducing a different chemical reactivity at the step. A step-flow growth mechanism occurs when adsorbed chemical species (*ad-species or adatoms*) on the surface terraces have sufficient energy to diffuse over the

terraces and eventually reach the step edges, where nucleation starts by aggregation to attachment sites.[35] In the case of 2D TMDs, it has been proposed that the step-flow growth mode can be promoted on vicinal sapphire templates by intentionally introducing a larger off-axis cut angle (**Figure S1-A**). Such periodic and pre-determined step topography can presumably guide TMD crystal growth into developing crystal domains with one preferred orientation provided you can enable the TMD nucleation on same side of the step across the sapphire surface **(Figure S1-B**).

On the contrary, a recent literature work claims that the dominant factor for the orientation of TMDs crystals relates to the epi-layer-template coupling on the reconstructed sapphire owing to attaining a similar atomic surface structure and stacking order across the sapphire surface terraces.[36] Sapphire surface reconstruction typically occurs at high temperatures and causes topographical- and thus structural- changes through a complex interplay of processes such as step coalescence, decomposition, bunching and faceting.[37,38] Moreover, such surface reorganization becomes more pronounced at larger off-axis cut angles (*i.e*., smaller terraces) [39,40] and therefore should indeed be taken into account when designing the deposition process. Given the high deposition temperature of most metal-organic and metal-oxide CVD processes of TMDs (>850 °C) and the distinct chemical reactivity of CVD precursors towards sapphire, the sapphire surface might reconstruct simultaneously with the adsorption and diffusion of the CVD precursors. On one hand, the step-flow growth mode might result in misoriented TMD domains when the sapphire surface develops faceted terraces during the (pre-)deposition process (**Figure S1-C**). On the other hand, if the sapphire surface reconstruction can be carefully understood and controlled, it may create an opportunity to achieve a single TMD crystal orientation through template and deposition process design.[41]

In this work, we disclose an alternative growth mechanism that results in a single crystalline molybdenum disulfide (MoS_2) monolayer through epitaxy on sapphire substrates with

intentionally different step and terrace structures. We analyze the crystal shape evolution of the MoS_2 crystals during the deposition process for different sapphire surface structures by Atomic Force Microscopy (*AFM*). As such, we determine the impact of the template surface topography and the template reconstruction on the MoS_2 crystal growth through the development of the additional MoS_2 crystal facets. We analyze the structure of the MoS_2 monolayer after coalescence by Transmission Electron Microscopy (*TEM*). We discuss the effect of surface steps on the MoS_2 crystal evolution and ultimately its influence on the closed monolayer structure and mobility.

Results and discussion

Sapphire surface topography induces MoS_2 crystal faceting during MOCVD

First, we investigate the relative contribution of (i) crystallographic symmetry provided by sapphire terrace surface and (ii) axial symmetry provided by sapphire topography (steps) when controlling the TMD crystal orientation. To answer this question, we analyze how the MoS_2 crystal orientation and shape evolves during various stages of the CVD process at 1000 ºC by intentionally varying the off-A axis cut angle of sapphire substrate. Molybdenum hexacarbonyl ($Mo(CO)_6$) and dihydrogen sulfide (H_2S) precursors are used to deposit the MoS_2 crystals by metal-organic CVD (*MOCVD*). We consider three types of c-plane sapphire templates with characteristic initial terrace widths ranging from a few nm to a few hundreds of nm, namely on-axis cut, 1° and 4° off-A axis cut sapphire (**Figure 1-A, B**). The first template type, on-axis cut sapphire, has been characterized in our earlier work and consists of large terraces ranging in width from 70 nm to few hundreds of nm and monosteps of 0.2 nm tall.[42] With the same 0.2 nm tall monosteps, the 1° and 4° off-A axis cut templates have the terrace width of around 12.4 nm and 3.1 nm, respectively. All the templates were used as received, without any additional pretreatment. The MoS_2 growth rate on sapphire is 0.006 ML/min by Rutherford

Backscattering Spectroscopy (*RBS*), irrespective of the sapphire surface structure and topography.

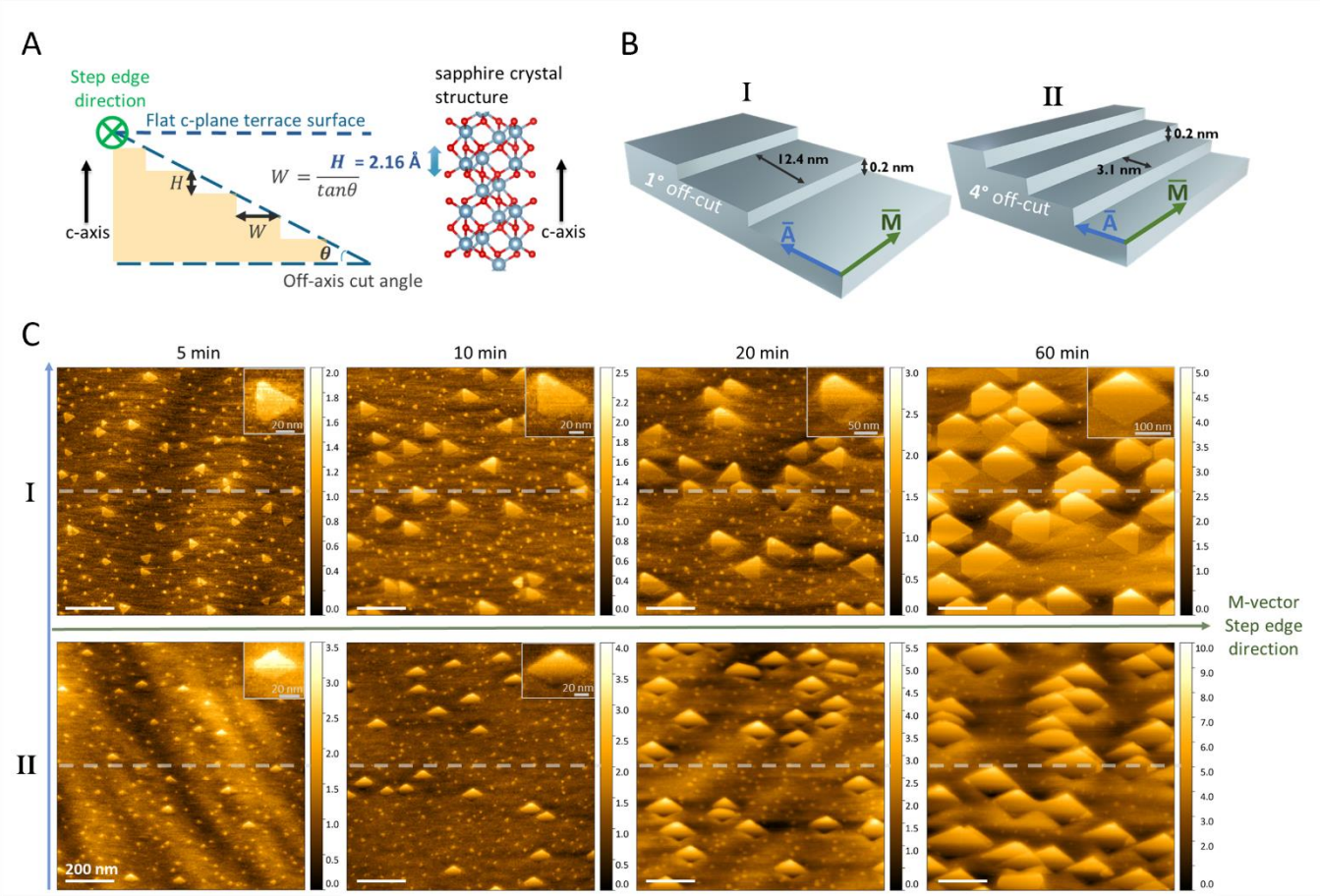

Figure 1. A - Sapphire step and terrace structure controlled by off-axis cut angle θ. The theoretical value of step height (*H*) between two terraces is 2.16 Å, as the distance between neighboring oxygen layers in the sapphire crystal structure (right). A formula to determine the theoretical terrace width (*W*) value is presented. **B** - The sapphire templates with 1˚ and 4˚ off-A axis cut angles used for MoS_2 growth. **C** - AFM images of 0.65 nm thick MoS_2 crystals deposited at 1000 °C on the 1° (**I**) and 4 ° (**II**) off-A axis cut sapphire at different deposition time (1000 °C, 75 Torr, H_2S and $Mo(CO)_6$ partial pressure is $1.9 \cdot 10^{-1}$ Torr and $5.8 \cdot 10^{-6}$ Torr, respectively). The height scale bar in nm is shown to the right after each image. The direction of A- and M-vector on sapphire c-plane is depicted by the blue and green arrows, respectively. The gray dashed lines correspond to the step edge orientation in the AFM images. During the

acquisition of AFM images, the scan direction is parallel to the flat of the sapphire wafer, ensuring M-vector lies in the horizontal plane of the AFM image. A height gradient over the MoS_2 crystals is caused by the image flattening and increases with the height difference between terraces on which the crystals are located, as described in detail in Supporting information.

The orientation of the MoS_2 crystals primarily originates from the crystallographic symmetry of the sapphire terrace rather than from the axial symmetry induced by the sapphire step edges, as illustrated in **Figure 1-C-I** for the MoS_2 crystals on the 1° off-A axis cut template during the deposition at 1000 ºC. For all studied off-A axis cut templates, the step edge is following the $[1\bar{1}00]$ direction (M-vector) of sapphire's c-plane. However, most MoS_2 crystals in the initial growth stage (after 5 minutes of deposition) are aligned along the $[11\bar{2}0]$ direction (A-vector), with both 0° and 60° rotated azimuthal orientation, as depicted in **Figure 2-A-1**. For the 1° off-A axis cut template, more than 85% of growing crystals align along A-vector of the bulk sapphire, as determined by AFM. This insight in the early growth stage is contrasting to the previous works, where the orientation of TMD domains is considered to be controlled by the step edge of the template, as the edges of TMD crystals were aligned along the step edge direction by AFM and/or Scanning Electron Microscopy.[30–34]

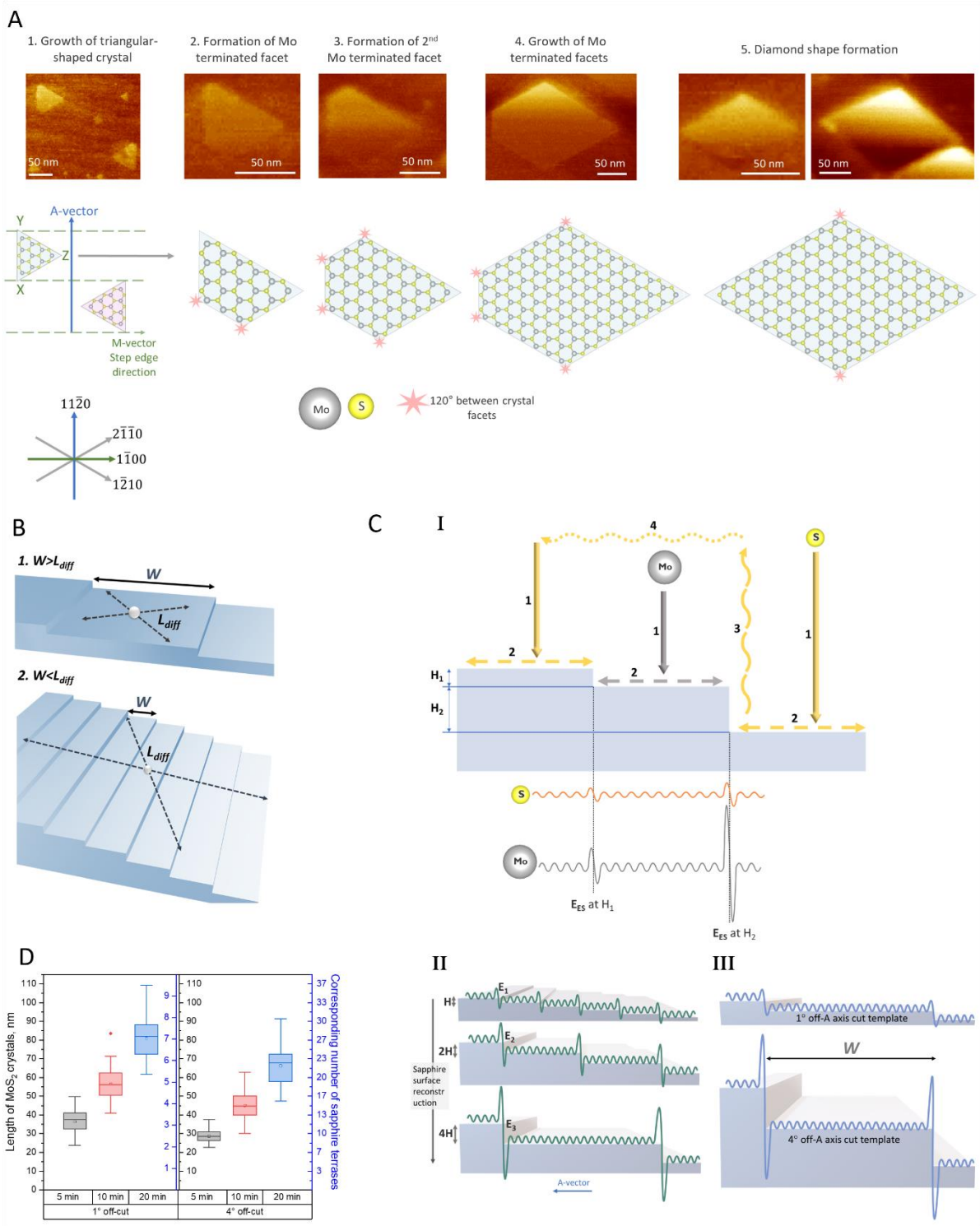

Figure 2. **A** – The stages of the MoS_2 crystal growth during the deposition process on off-A axis cut sapphire. Top - the zoomed in MoS_2 crystals from Figure 1-C; step 1, 2, 3, 4 corresponds to 5 min, 10 min, 20 min, and 60 min in Figure 1-C-I, respectively; left and right images in step 5 correspond to 10 min and 60 min in Figure 1-C-II, respectively. Bottom – corresponding schematics that represent the MoS_2 crystal shape evolution. The stars indicate

angles of 120°. **B** – Possible relation between terrace width W and the average diffusion length of adatoms L_{diff} on the template with a step and terrace topography. **C-I** – Top: possible diffusion path for Mo (grey) and S (yellow) adatoms: 1 – adsorption, 2 – surface diffusion, 3 – desorption, 4 – gas phase diffusion. Bottom: schematical representation of Ehrlich-Schwoebel barrier (E_{ES}) for surface diffusion of Mo and S adatoms on surface consisting of steps and terraces along A-vector. E_{ES} is determined by the step height. The distinct difference in diffusional transport and adatom concentration on the surface between Mo and S can play a key role in how the crystal shape develops as a function of the sapphire topography. **II** - An increase of the potential barrier induced by the increase of the step height during sapphire surface reconstruction. **III** – Visual comparison of Ehrlich-Schwoebel barrier for the 1° and 4° off-A axis cut template for the same terrace width. The difference in the barrier height is caused by the difference in the step height. **D** - The length of the MoS_2 crystals along A-vector on the left axis (black) versus deposition time of 5, 10 and 20 min on the 1° and 4° off-A axis cut templates at 1000 ºC. The equivalent theoretical number of sapphire terraces before their reconstruction that are covered by the crystals is presented as the right axis (blue) for each template.

Markedly, the sapphire surface topography affects the MoS_2 crystal shape rather than the crystal orientation during the MOCVD process (**Figure 1-C**). Therefore, we analyze how the MoS_2 crystal shape evolves with the MoS_2 deposition time to further elucidate the growth mechanism. Initially, the growing MoS_2 crystals have a triangular shape, which is typical for deposition processes with a high partial pressure ratio between sulfur and molybdenum precursors.[43] The higher amount of available sulfur species for the growing crystal leads to an unequal growth rate of the molybdenum and sulfur terminated edges, resulting in deviation from the hexagonal crystal shape, which correspond to MoS_2 crystalline structure, and the development of triangular crystals.

Interestingly, the original triangular shape of the MoS_2 crystal, observed after 5 min of deposition on the 1° off-A axis cut template, changes with the deposition time. This is as opposed to the growth on the on-axis cut template, where the triangular shape remains preserved throughout the deposition process (**Figure S2**). **Figure 2-A** depicts the proposed structures that can account for the shape evolution of the MoS_2 crystals on off-axis cut sapphire by combining AFM observations with the crystallographic structure of 1H-MoS_2. Here we assume that the orientation of the lattice does not change. For the initial triangular crystals, the edge termination varies from sulfur to molybdenum during the deposition process. For simplicity, we represent the crystals at the moments when the original triangular crystal facets, presented in **Figure 2-A-1**, are sulfur terminated in zigzag edge configuration, which is considered to be the most stable.[26,44] The first deviation from the triangular shape is observed for some crystals already after 5 min of deposition, and after 10 min of deposition the majority of the MoS_2 crystals develop an additional facet (**Figure 1-C-I**). The facet is formed at the edges of the MoS_2 crystal propagating along A-vector of sapphire towards the step edge, *i.e.*, either at X or Y edge of the triangle depicted in **Figure 2-A-1**. Interestingly, the first facet always develops at the same edge of the crystal, X edge in the presented case in **Figure 2-A**. This also implies that if for 0° rotated crystals X edge is located in the bottom of the crystal, then for 60° rotated crystals this edge is located at the top of the crystal, and in this case the first facet develops at the top, consistent with the AFM images in **Figure 1-C-I**. This newly created facet forms an angle of 120° with the neighboring sulfur terminated facets that corresponds to the molybdenum terminated facet in zigzag configuration, according to the crystallographic structure of MoS_2 (**Figure 2-A-2**). Later, the second Mo-terminated facet is formed at Y edge, *i.e.*, the second edge of the crystal, which propagates along the A-vector of sapphire towards the step edge (**Figure 2-A-3**). MoS_2 crystal with two developed Mo-terminated facets is the most observed shape after 20 min of deposition (**Figure 1-C-I**). During

further growth, the newly formed Mo-terminated facets grow faster than a S-terminated facet located between them, resulting in a truncated diamond crystal shape that is the dominant shape after 60 min of deposition (**Figure 2-A-4, Figure 1-C-I**). As a next step, we expect that the diamond shaped crystals will form (**Figure 2-A-5**). However, the MoS_2 crystals grown on the 1° off-A axis cut template start to coalesce before the predicted shape can emerge.

Notably, only the X and Y crystal edges of MoS_2, which are oriented perpendicular to the step edge direction of the sapphire template, become faceted and according to our hypothesis Mo-terminated. The third crystal edge Z, oriented along the terrace, does not develop any additional facets. Thus, the observed deviation from the triangular MoS_2 crystal shape during the deposition process on the 1° off-A axis cut template is anisotropic and demonstrates the impact of the template topographical structure on the crystal growth. During CVD, the crystal growth is governed by a complex interplay of different processes such as precursor adsorption that results in the formation of ad-species. These ad-species can diffuse over the surface, resulting in reversible desorption, reflection or aggregation at step edges or aggregation at MoS_2 crystals and lattice incorporation.

On the templates with topographical features, such as the sapphire steps, the relation between adatom diffusion length (L_{diff}) and terrace width (W) is an important parameter in the deposition process (**Figure 2-B**). If the terrace width exceeds the diffusion length, $W > L_{diff}$, the probability of adatoms reaching a step edge is low, and the influence of the template topography on the growth process will be limited. On the other hand, if the terrace width is smaller than the diffusion length, $W < L_{diff}$, the adatoms will have a high probability to encounter the step edges during their lifetime. In this case, the diffusion path of the adatoms can be altered as compared to that on a planar surface, as will be discussed further.

To better understand the growth mechanism during MoS_2 CVD, we first estimate the average adatom diffusion length from the interdomain distance $L_{diff} \approx I_d$ according to the method

described in the reference [45] (**Table 1**). For this approximation, the first condition $W > L_{diff}$ is satisfied when depositing MoS_2 on the on-axis cut sapphire template. As a result, the template topography imposes little effect on the MoS_2 crystal shape evolution and the MoS_2 crystals remain triangular during the steady-state growth regime, consistent with the AFM results. By contrast, for the larger off-A axis cut templates (i.e., 1° and 4°), the MoS_2 growth proceeds under boundary conditions where $W < L_{diff}$ applies. The template topography more profoundly affects the overall MoS_2 deposition process as the diffusion of ad-species over the step edges is less favorable, consistent with the observed shape deviation on the 1° and 4° off-A axis cut templates.

Table 1. As-received sapphire template properties that describe step and terrace structure versus MoS_2 growth behavior at different deposition temperatures.

Template	Step height H, nm	Terrace width W, nm	Growth T, °C	Interdomain distance (I_d), nm	Ratio I_d/W	MoS_2 growth behavior
on-axis cut	0.2	102	1000	50	0.5	Controlled by sapphire template bulk
1° off-A axis cut	0.2	12.4	1000	56	4.5	Slow evolution to diamond shape
4° off-A axis cut	0.2	3.1	1000	55	17.7	Fast evolution to diamond shape
on-axis cut	0.2	107	850	20	0.2	Controlled by sapphire template bulk
1° off-A axis cut	0.2	12.4	850	30	2.4	Start of shape evolution but mostly controlled by sapphire template bulk
4° off-A axis cut	0.2	3.1	850	28	9.0	Shape is controlled by step edges

Interdomain distance was calculated from the experimental data in the approximation of isotropic growth in the steady state regime.

The presence of atomic steps on the template surface is known to give rise to an Ehrlich-Schwoebel potential barrier (E_{ES}) near the step edges, thus affecting the surface diffusion of adatoms.[46,47] The height of the E_{ES} barrier varies between different ad-species and increases with the increase of the step height (**Figure 2-C**). We therefore propose that the sapphire

surface with the high density of surface steps act as a barrier for surface diffusion of precursor ad-species, resulting in accumulation or reflection of the ad-species from the step edge. As a result, this leads to an overall anisotropic ad-species flux in the direction of the edges. The effect of the Ehrlich-Schwoebel barrier can be different for Mo and S adatoms because of their different diffusion pathways **(Figure 2-C-I)**. In general, for CVD process, it is expected that adsorbed precursor species can eventually desorb with a certain probability. However, the use of metal organic precursor $Mo(CO)_6$ above its decomposition temperature implies that the metal precursor adsorption is almost irreversible. Hence, surface diffusion is a dominant diffusion pathway for Mo ad-species.[48] On the other hand, due to the comparatively higher vapor pressure of S species, S species can desorb and further pursue gas-phase diffusion, leading to shorter lifetime on the surface and reversible adsorption (**Figure 2-C-I**). As a consequence of this distinct difference in diffusional transport and Ehrlich-Schwoebel barrier depending on the type of Mo and S ad-species, the concentration and spatial distribution of those adatoms can differ near the step edges.

Therefore, we hypothesize the accumulation of Mo adatoms near the terrace edge during the deposition process. The MoS_2 crystals might nucleate at the step edge or on the terrace. Either way, when they approach the accumulation site, the energy of Mo-terminated edge formation decreases.[49] This can explain the MoS_2 crystal shape change and its dependence on the sapphire topography as well as the development of additional facets in the MoS_2 crystals. Finally, sapphire surface reconstruction during the deposition process with coalescence of terraces gives rise to the higher step edges with the higher potential barrier for the ad-species. As a result, if $W << L_{diff}$ condition is applied, the precursor flux anisotropy will be amplified (**Figure 2-C-II**). For the on-axis cut template, the development of the additional crystal facets is generally not observed because of the much larger terrace width meaning less impact of anisotropic diffusion and deviations related to the surface steps. For the 1° off-A axis cut

templates, $L_{diff} \approx 4.5$ W, indicating a significant influence of step edges on the surface diffusion of Mo adatoms and affecting the MoS_2 crystal shape evolution (**Table 1**). Moreover, the sapphire surface simultaneously reconstructs during the MoS_2 deposition increasing both the terrace width and step height, and concomitantly raising E_{ES} (**Figure 2-C-II**). The higher E_{ES} barrier compensates for induced terrace widening and, as a result, anisotropic growth is preserved. The effect of narrower starting terraces and larger L_{diff}/W ratio on the anisotropic metal precursor diffusion is discussed in the next paragraph.

To further investigate the proposed mechanism and the impact of the template's stepped surface structure on MoS_2 growth mode, we analyze the shape evolution of the MoS_2 crystals grown on the 4° off-A axis cut template. In contrast to the 1° off-A axis cut template, with its nominal terrace width of around 12.4 nm, the 4° off-A axis cut template has a starting terrace width of around 3 nm. Hence, the 4° off-A axis cut template possesses the higher density of the surface steps with initial $L_{diff}/W \approx 17.7$. This template experiences faster surface reconstruction, and higher steps are formed earlier in the deposition process, as compared to the 1° off-A axis cut template. Thus, E_{ES} barrier is higher for Mo adatoms on the surface of the 4° off-A axis cut template due to the taller steps, with terraces' width smaller or approaching the ones of the 1° off-A axis cut template (**Figure 2-C-III**). Consequently, according to the proposed mechanism, we would expect a more pronounced impact of anisotropic surface diffusion in A-vector direction on crystal growth for the 4° off-A axis cut template.

Indeed, after 5 min of deposition at 1000 ºC on the 4° off-A axis cut template, the largest MoS_2 crystals already have the characteristic truncated diamond crystal shape corresponding to step 4 in **Figure 2-A** (**Figure 1-C-II**). The newly formed Mo-terminated facets have grown faster than the S-terminated facet in between of them. At the same time, the smaller crystals are triangular, or of an unidentified shape due to their small size (**Figure 1-C-II**). Further in the deposition process on the 4° off-A axis cut template, the Mo-terminated facets overgrow

the S-terminated facet in between, thus forming the MoS_2 crystals of diamond shape, which was not observed in the case of the 1° off-A axis cut template (step 5 in **Figure 2-A**, **Figure 1-C-II**, after 10 min of deposition). The formed diamond shape of MoS_2 crystal does not further change in shape but increases in size until the grains' coalescence, being the stable configuration of MoS_2 crystal with altering edge termination, namely, Mo-, S-, S-, Mo-terminated (**Figure 1-C-II**, after 20 and 60 min of deposition). As a result, the first three steps of the crystal shape evolution occur much faster on the 4° off-A axis cut templates, revealing the grown Mo-terminated facets in the beginning of the deposition process.

To further illustrate the differences in MoS_2 crystal shape evolution in the initial stage on the 1° and 4° off-A axis cut templates, the length of MoS_2 crystals along the A-vector is compared to the corresponding theoretical number of sapphire terraces that are covered by the crystals (**Figure 2-D**). As sapphire terraces coalesce during the deposition process, resulting in higher step edges, comparing the nominal number of terraces covered by the MoS_2 crystals between the templates indirectly indicates the relative difference in the number of steps. For the 1° off-A axis cut template after 5 min of deposition, the triangular crystals are covering about 2 to 4 nominal terraces. Note that only a slight reconstruction is expected for this template because of the short deposition time. In the later stage, after 10 min of deposition, up to 6 terraces are covered by one MoS_2 crystal, and at this stage the first Mo-terminated facet evolves. After 20 min of deposition, when the MoS_2 crystals are mostly located on the equivalent area of 7 terraces, the crystals have already developed one or two Mo-terminated facets. In contrast, for the 4° off-A axis cut template, the majority of crystals are already covering 9-10 terraces after only 5 min of deposition due to the smaller nominal terrace width.

To summarize, the MoS_2 crystal shape evolution on the 4° off-A axis cut template proceeds faster as compared to the 1° off-A axis cut template because of the initial difference in the terrace width for these two templates. The higher number density of sapphire step edges

induces pronounced anisotropy in the Mo adatom diffusion already during the early stages of the deposition process. Furthermore, shorter terraces of the 4° off-A axis cut template are subject to faster surface reconstruction, leading to higher steps and raising the E_{ES} barrier. Thus, the E_{ES} barrier becomes higher for the same terrace width as compared to the 1° off-A axis cut template (**Figure 2-C-III**). This explains why the MoS_2 crystals on the 4° off-A axis cut template already form Mo-terminated facets this early in the deposition process, and earlier than on the 1° off-A axis cut template.

The effect of reduced template surface reconstruction on MoS_2 crystal faceting

As demonstrated in the previous section, the topographical change of the sapphire surface during its reconstruction at high deposition temperature can have a substantial impact on the MoS_2 crystal shape evolution. Next, we study if and how topography affects crystal shape at the MoS_2 deposition temperatures where sapphire surface reconstruction is much slower by decreasing the deposition temperature to 850 °C. The impact of lower deposition temperature on sapphire surface topography is discussed in Supporting information (**Figure S3** and **Figure S4**). During the 850 °C deposition process, all other deposition parameters are kept identical to 1000 °C deposition (see Materials and Methods). Practically, deposition temperature decrease will also affect the relative adsorption and diffusion kinetics of the MoS_2 process, in addition to the impact on surface reconstruction.

Throughout the deposition process at 850 °C, the growth rate and the amount of deposited material is not different from 1000 °C, as characteristic for a mass-transport limited growth regime and confirmed by RBS (**Figure 3-A**). In spite of the similar growth rate, the number of crystals per unit area (areal density) of MoS_2 increases with the decrease of the deposition temperature (**Figure 3-B**). The crystals deposited at 850 °C are much smaller and are present in larger amounts compared to higher temperature deposition (**Figure 3-C** and **Figure 3-D**). The described difference in crystal density between different deposition temperatures is not

surprising for the selected deposition chemistry. Assuming that crystals grow mainly by surface diffusion and aggregation of ad-species, the areal density of crystals is determined by the diffusion length of metal ad-species on the surface, which depends on the deposition temperature, so it can explain areal density evolution with the deposition temperature.

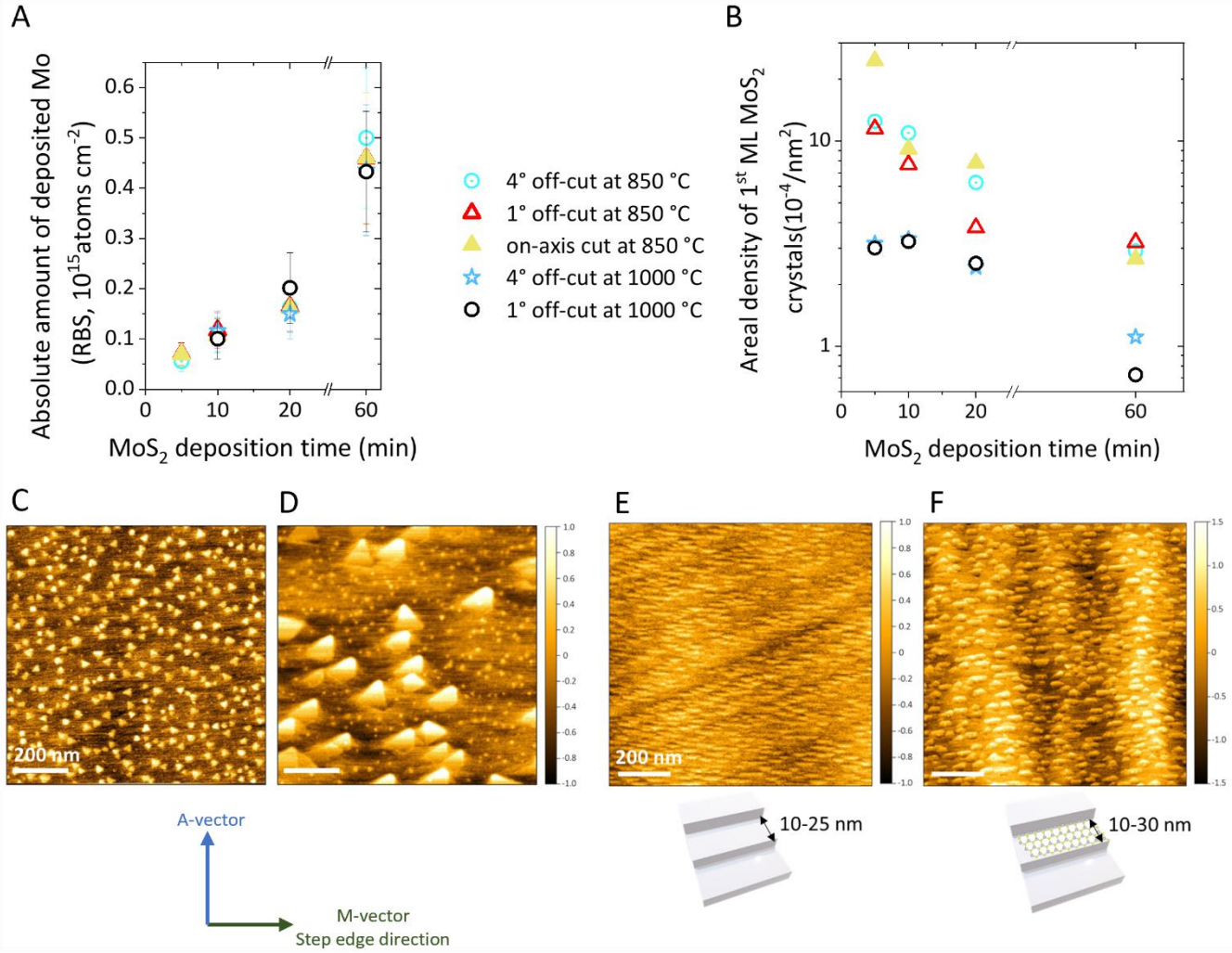

Figure 3. **A** - The absolute amount of deposited molybdenum increases linearly with MoS_2 deposition time, as measured by RBS. **B** - The higher areal density of the MoS_2 crystals at lower deposition temperature (850 °C) compared to 1000 °C deposition. Calculated from AFM images. The areal density of crystals is not affected by the type of template at a given deposition temperature. **C** and **D** - AFM imaging of the MoS_2 crystals deposited on sapphire the 1° off-A axis cut template after 20 min of MoS_2 MOCVD. Deposition at (C) - 850 °C, (D) - 1000 °C. **E**

- Surface topography of the 4° off-A axis cut sapphire after annealing at 850 °C in H_2S for 60 min. **F** – The MoS_2 crystals grown at 850 °C for 60 min on the 4° off-A axis cut template. The direction of sapphire A- and M-vector is given at the bottom left for C-F.

Despite the minimization of topography changes related to sapphire surface reconstruction at 850 °C, the template topography still influences the development of MoS_2 crystals during the deposition process (**Figure S5**). The precise crystal shape analysis is challenging for the MoS_2 crystals grown at 850 °C, as the crystals are much smaller than those grown at 1000 °C. Nevertheless, throughout the deposition process, the triangular MoS_2 crystals on the on-axis template are larger compared to the crystals grown on the 1° off-A axis cut templates, where their development is affected by the presence of the step edges (**Figure S5-A, -B**). For deposition at 850 °C, the L_{diff}/W ratio drops to 2.4 for the 1° off-A axis cut sapphire, consistent with the slower diffusion of ad-species at the lower deposition temperature (**Table 1**). As such, the influence of the step edges on the anisotropic crystal growth is expected to become less pronounced than for deposition at 1000 °C. Indeed, only few MoS_2 crystals on the 1° off-A axis cut template develop an additional facet during the growth while the majority stays triangular till 60 min of deposition. The size of those crystals stays relatively small, not exceeding 30 nm as a triangle side after 20 min of deposition at 850 °C, while for the crystals deposited at 1000 °C this value is around 40 nm only after 5 min of deposition.

At the same time, the MoS_2 crystals on the 4° off-A axis cut template remain strongly affected by the template topography (**Figure 3-F, Figure S5-C**). On the one hand, a pronounced influence of anisotropic adatom diffusion on the crystal shape is expected for L_{diff}/W ratio of 9.0 and given 4° off-A axis cut templates reconstruct comparatively faster. Indeed, many of the MoS_2 crystals on the 4° off-A axis cut template develop the additional facets, seen after 20 min. On the other hand, crystal overgrowth over the steps is another important aspect that can affect MoS_2 growth. After 20 min of deposition at 850 °C on 4° off-A axis cut template, we

observe crystals that propagate along the terrace instead of overgrowing the step edge, in addition to the development of faceted crystals. The growth along the terrace edges continues during the further deposition process (**Figure S5-C**, after 60 min). So, the hypothesis proposed above, *i.e.*, anisotropic diffusion of ad-species induced by the template's step and terrace topography, is consistent with the observations at the lower deposition temperature: the topography of the template affects the MoS_2 shape evolution and anisotropic shapes are observed. However, the origin of the elongated crystals on the 4° off-A axis cut template is investigated further.

Next, we verify the impact of surface reconstruction by an anneal experiment, where we investigate how the substrate surface topography changes for representative process conditions in the absence of MoS_2 deposition (**Figure 3-E**). As a result of annealing in H_2S for 60 min at 850 °C of the 4° off-A axis cut template, the terraces with the width of 10-25 nm measured along A-axis are formed, separated by the steps of around 1 nm, indicating the coalescence of 3-8 terraces on the as-received template (**Figure 3-E**). The terrace width of 10-25 nm corresponds to the dimension of the MoS_2 crystals after 60 min of growth, measuring 10-30 nm. This confirms that the growth of the MoS_2 crystals is limited to propagate in the A-vector direction by the high step edges of sapphire. Moreover, the width of the terrace reaches the approximate average ad-species diffusion length value $W \approx L_{diff}$ (25 nm *vs* 28 nm, respectively). Consequently, the probability of reaching the step edge by adatoms is reduced. As a result, the crystals are spreading faster along the terrace than across the step edges. (**Figure 3-F**).

Thus, the reduction of the deposition temperature to slow down the surface reconstruction rate results in a different effect on the growth evolution of the MoS_2 crystals dependent on the template. On one hand, the MoS_2 crystals on the 1° off-A axis cut template do not experience a pronounced influence from the template topography due to their small size and the limited

impact of template reconstruction during the first 60 min of the deposition at 850 °C. On the other hand, the development of the MoS_2 crystals on 4 ° off-A axis cut template is strongly controlled by the topographical features, formed during the reconstruction. Still, for both templates the observed shape evolution is consistent with the hypothesis of anisotropic surface diffusion of ad-species, as proposed above. Hence, the geometry of MoS_2 crystal's shape can be controlled by means of carefully modulating the surface topography and the type of diffusional transport mechanism, *i.e.*, surface versus gas-phase diffusion, *e.g.*, through the deposition temperature, the precursor dose, and the gas composition.

Formation of single crystalline MoS_2 monolayer with state-of-the-art mobility values

To assess how the observed growth mode affects the properties of the closed monolayer, the MoS_2 crystalline quality is characterized. First, the deposited MoS_2 monolayers demonstrate the typical peaks positions for photoluminescence and Raman spectra (**Figure S12, S13**). Then, in-plane Grazing Incidence X-Ray Diffraction (*GIXRD*) for $(11\bar{2}0)$ plane of MoS_2 is recorded, revealing the epitaxial alignment of $(11\bar{2}0)$ plane of MoS_2 with $(11\bar{2}0)$ sapphire plane for both deposition temperatures (**Figure 4**). Moreover, the peaks at -60°, 0° and 60°, without the intermediate rotated domain, are present, indicating a high crystalline quality of the deposited MoS_2. We can compare the Full Width at Half Maximum (*FWHM*) of the in-plane diffraction peaks for MoS_2 deposited on sapphire to established literature as a benchmark for epitaxial growth. The XRD FWHM is a convoluted measure of (i) the tilt or mosaicity of the (-110) crystallographic plane, (ii) the crystal lattice deformation due to strain induced by the epitaxial relationship of MoS_2 monolayer with sapphire (hence governed by the sapphire terrace and step structure and surface reconstruction), and (iii) the crystal domain size.

The measured FWHM for MoS_2 monolayers deposited at 1000 °C on the on-axis cut sapphire templates is around 0.3°, indicating a low level of grain misorientation in the MoS_2 monolayer. This value is slightly higher than that for the single crystalline sapphire substrate (0.2°). The

FWHM of MoS_2 is in agreement with the previous reports in literature for the epitaxially deposited MoS_2 monolayers on c-plane sapphire (0.3°). [50] Moreover, similar values were measured for other epitaxially grown 2D TMDs on c-plane sapphire, for example, 0.4° for WS_2 [23] and 0.28° for WSe_2.[51] A recent paper notably reports much narrower FWHM values, namely 0.09° for single crystalline WS_2 grown in a multistep process, and 1.13° for a WS_2 monolayer grown at 850 °C.[33]

Furthermore, we also observe peak broadening for MoS_2 deposited on the on-axis cut sapphire when the deposition temperature decreases from 1000 °C to 850 °C, presumably due to the smaller crystallite size and possible presence of misoriented domains at lower deposition temperature. Please note that for aforementioned literature works the sapphire off-cut angle of was not reported, thus we use the on-axis cut sapphire to enable comparison with literature.

The XRD peak broadening for the higher off axis cut angles might be convoluted by a variety of factors. First, the MoS_2 CVD precursor chemistry determines how the sapphire surface reconstructs, resulting in different sapphire surface topographies (*i.e.*, terrace width and height) between the reported MoS_2 deposition processes in literature and for the MoS_2 monolayers grown on the 1° and 4° off-A axis cut templates reported in this work. Sapphire surface topography brings an additional aspect that can influence the XRD peak widths. For example, the sapphire surface reconstruction can induce strain or even tilt the crystallographic MoS_2 planes broadening the FWHM. Second, as the sapphire surface reconstruction is temperature dependent, it is a factor that cannot be excluded when comparing XRD spectra as a function of the MoS_2 MOCVD deposition temperature and off-axis cut angle. Thus, to have a further reliable and complementary indication of the MoS_2 domain size and orientation on the 1° and 4° off-A axis cut templates, electron diffraction proves vital.

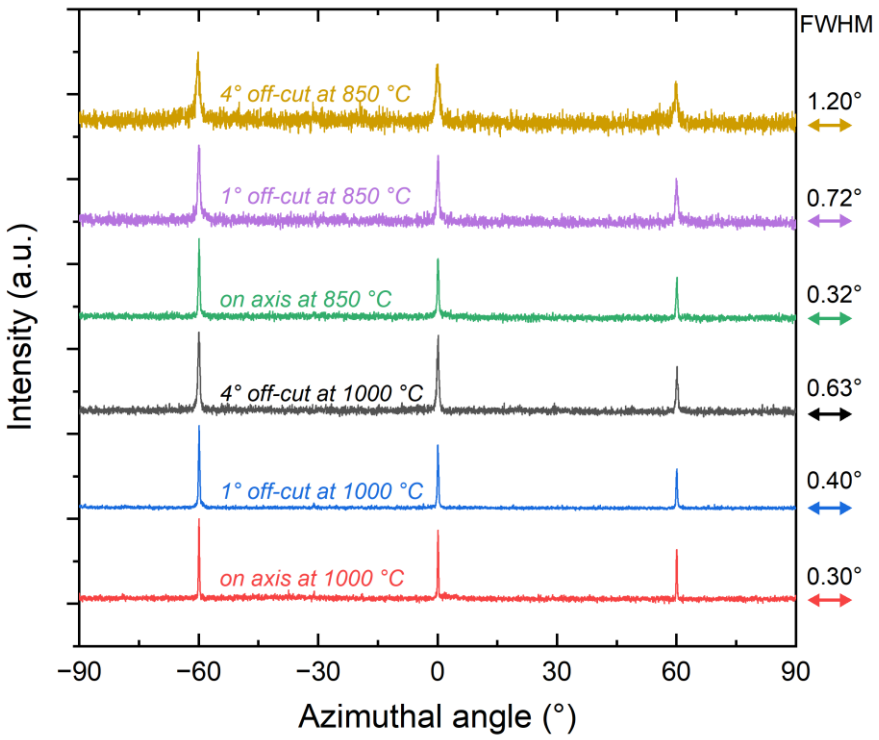

Figure 4. In plane GIXRD φ-scan of the closed MoS_2 monolayer. The average full width at half maximum (*FWHM*) of the peaks for each plot is indicated to the right.

For the separate crystals in the beginning of the deposition process, AFM images above demonstrate 0° and 60° geometrical rotation of the deposited crystals, whose rotation during the deposition process is not expected, as those crystals are already in the minimum energy position. In the 1 μm by 1 μm field of AFM view, among the crystals oriented along A-vector of sapphire, the observed number of 60° rotated domains (twins) is ranging from 7 to 36 %, as determined from 12 AFM images of MoS_2 grown on the 1° off-A axis cut sapphire. Thus, upon the layer coalescence, it is generally expected to see the monolayer consisting of the 0° and 60° rotated domains, like in previous works.[51–53] On the contrary, plan-view Transmission Electron Microscopy *(TEM)* demonstrates that the large area single crystalline monolayer is formed upon the layer coalescence, indicating the seamless stitching of the diamond-shaped MoS_2 domains (**Figure 5**). Interestingly, the single crystalline MoS_2 is observed on the large area of

at least 50 µm by 50 µm (**Figure S7**), while the lateral dimension of the MoS_2 domains right before the coalescence did not exceed 200 nm. There are three possible mechanisms behind the formation of the single crystalline MoS_2 monolayer: first, the observed geometrically 0° and 60° rotated crystals (by AFM) might have the same lattice orientation, in this case no rotated domains are present during the MoS_2 domains growth. The second possible mechanism assumes the presence of 60° rotated domains during the growth, this mechanism can take place during the MoS_2 layer coalescence and is responsible for reorientation or ripening of 60° rotated crystals. Such phenomenon was observed for other 2D materials, *e.g.*, graphene, however it has never been reported for 2D TMDs.[54] The third possible mechanism is the Mo or S plane gliding in the closed monolayer, which can lead to the 2H to 2H' phase transition, as described elsewhere.[55] Crystallization upon layer coalescence is subject to further study.

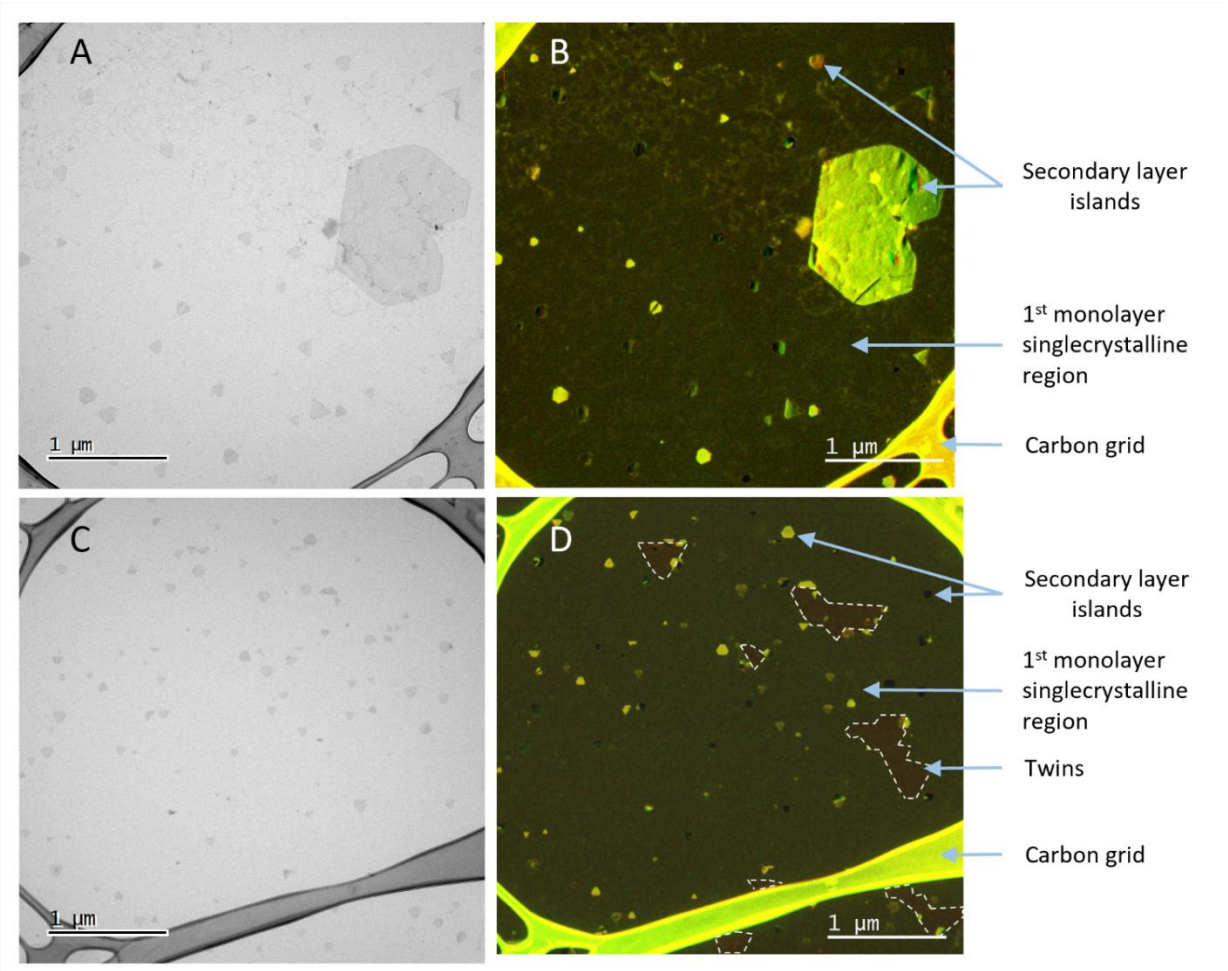

Figure 5. TEM images of the MoS_2 monolayers transferred on carbon grid. **A** and **C** correspond to bright field TEM, **B** and **D** are the combination of two dark field TEM images in false colors, see **Figure S6**. The MoS_2 monolayers are grown at 1000 °C on the 1° off-A axis cut template (A-B) and on the 4° off-A axis cut template (C-D). The 60° rotated twins are indicated in D using dashed lines.

Still, there is an influence of the template on the MoS_2 monolayer's crystalline structure, as indicated by TEM analysis. MoS_2 grown on the 1° off-A axis cut template is single crystalline in large area and no 60° rotated domains are detected in the layer, while the growth on the 4° off-A axis cut template results in around 5% of the 60° rotated twins in the monolayer, as determined from the visible area of 5 µm by 5 µm image (**Figure 5-D**). The large area 50 µm by 50 µm montage TEM images (**Figure S7, S8**) and 5 µm by 5 µm TEM images from various regions of the samples (**Figure S9, S10**) confirm that the images in **Figure 5** are representative for the deposited MoS_2 monolayers.

The appearance of 60° rotated domains in the MoS_2 monolayer grown on the 4° off-A axis cut template might originate from the different stage of the crystal shape evolution during the domain's coalescence. As discussed in the previous part, the MoS_2 domains grown on the 1° off-A axis cut template start to coalesce before reaching the stable diamond shape, possibly making the reorientation of the 60° rotated domains more energetically favorable during the coalescence process. On the other hand, if grown on the 4° off-A axis cut template, the separate domains are in the stable diamond shape before the coalescence, increasing the required energy for domains reorientation while merging with the neighboring domains. Still, the mechanism of 60° rotated crystals reorientation is not understood and must be further studied in more detail.

Next, we investigate the impact of the MoS_2 crystallinity grown on the 1° off-A axis cut template (single crystalline) and the 4° off-A axis cut template (single crystalline with some

remnant 60° rotated domains) on the MoS_2 monolayer electrical performance by fabricating MoS_2 back-gated field-effect transistors (**Figure 6**). Prior to the device fabrication, the MoS_2 monolayer is transferred on 50 nm SiO_2/p^+-Si substrates by wet transfer. The transfer process together with the device fabrication details are published elsewhere. [42] Here we report the long channel devices of 20 μm in order to eliminate the impact of the contact resistance on the extracted mobility values. Nevertheless, the performance of the devices for the shorter channels is reported in Supporting information (**Figure S11-A**). The measured devices demonstrate a large on/off current ratio that reaches 10^8. Interestingly, the performance of MoS_2 from the 1° off-A axis cut sapphire is better compared to the one grown on the 4° off-A axis cut sapphire (**Figure 6**). If calculated using transfer length method (*TLM*), the MoS_2 mobility from the 1° off-A axis cut template reaches 26 $cm^2 V^{-1} s^{-1}$ while the value is around 14 $cm^2 V^{-1} s^{-1}$ for MoS_2 from the 4° off-A axis cut template, suggesting the negative impact of the 60° rotated twin boundaries in the first monolayer on the electrical performance (**Figure S11-B**). This trend is also reflected in two-point probe (*2PP*) mobility, where MoS_2 from the 1° off-A axis cut template demonstrates a mean mobility of around 25 $cm^2 V^{-1} s^{-1}$ with the best performing devices reaching 28 $cm^2 V^{-1} s^{-1}$ (**Figure 6-C**). These mobility values correspond to the current state of the art field effect mobility for the similar MOCVD grown MoS_2 monolayers on sapphire and are comparable with MoS_2 mobilities grown on SiO_2 with MOCVD (**Figure 6–D**).[50,56–60] So far, we attribute the difference in the highest extracted carrier mobility between our work and the literature on NaCl-promoted MOCVD[58] to the intra-grain defectivity.

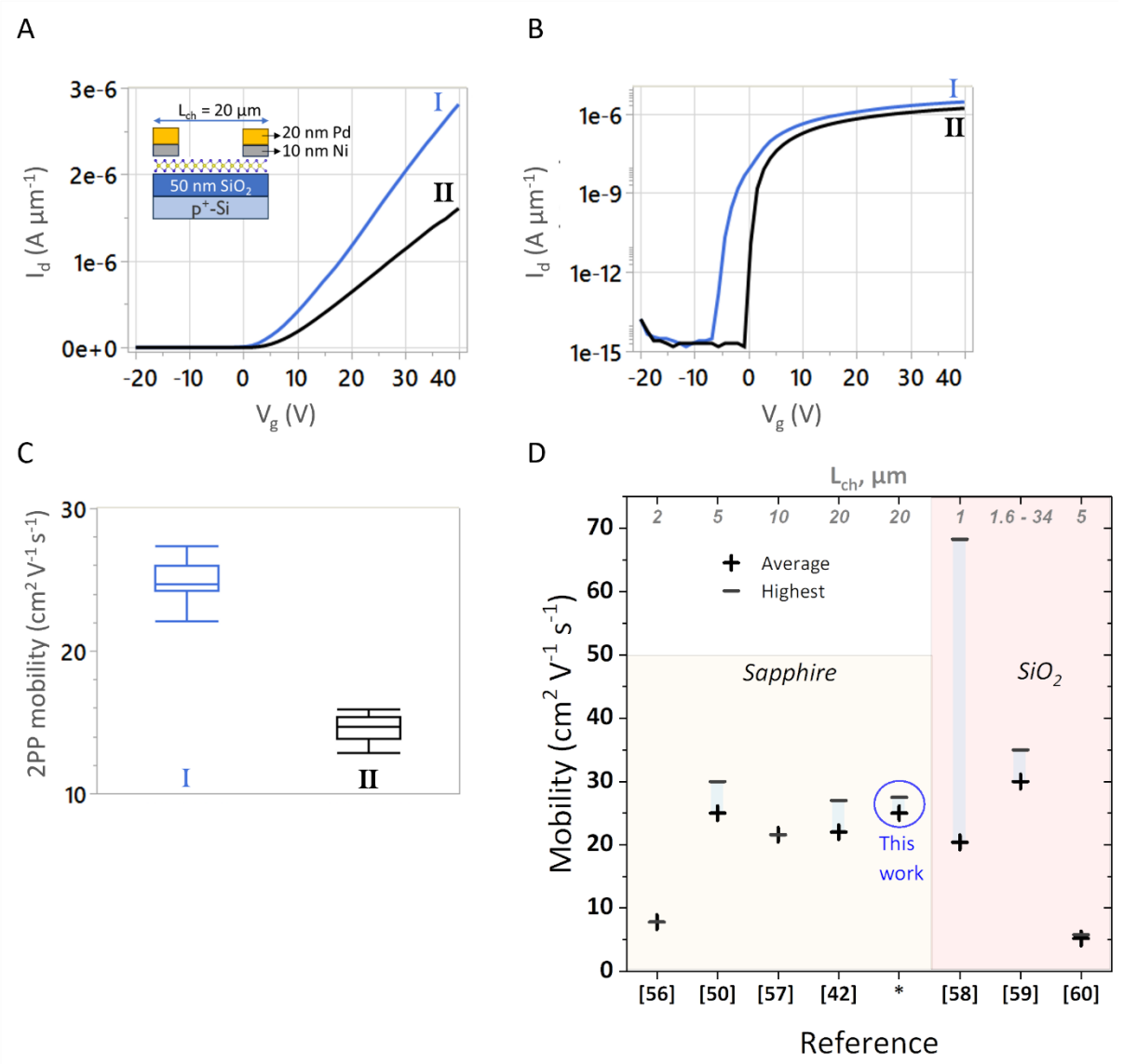

Figure 6. Electrical performance of the MoS_2 monolayers grown on the 1° (I – in blue) and 4° (II – in black) off-A axis cut template. The inset in (A) depicts the structure of the devices, channel width for all devices is 100 µm. Drain current (I_d) versus gate voltage (V_g) transfer characteristics are presented in linear (**A**) and logarithmic (**B**) scale for drain voltage (V_d) of 1V. **C** - 2PP mobility of charge carriers. **D** – Mobility benchmark for MoS_2 grown by MOCVD process on sapphire (left) and SiO_2 (right). The average, the highest mobilities, and the channel length are indicated. Note, in [57] an aqueous solution of sodium molybdate (Na_2MoO_4) is used as a metal precursor, in [58] NaCl promotor is used, in [60] gas-phase alkali metal-assisted MOCVD is employed.

Conclusions

Researchers have been investigating for decades how to control and guide the growth of various materials by substrate design via lattice structure, topography, chemical or phase contrast, for a variety of applications in micro/nano-processing, nanotechnology, catalysis, *etc.* Mechanistic understanding can guide the rational design of deposition processes with ultimate growth control.[61–63] Here, we provided insight into the influence of substrate topography on growth behavior of 2D crystals, exploring topography induced anisotropic growth and crystal shape modulation. This work revealed a growth mechanism during MoS_2 CVD that leads to a single crystalline MoS_2 semiconductor monolayer on sapphire templates with a step and terrace surface topography through anisotropic crystal growth. In the early crystal growth stage, the crystal's orientation was controlled by the epitaxial relationship, thus resulting in 0 º and 60 º rotated triangular domains. However, during further growth, the crystals approached a diamond shape through formation of additional crystal facets. The evolution from triangular- to diamond-shaped MoS_2 crystals was attributed to anisotropic diffusion of ad-species on templates with nanoscale step and terrace structure, which can be enhanced by template surface reconstruction during growth. Upon MoS_2 monolayer coalescence, the formation of single crystalline MoS_2 monolayer on sapphire templates is detected. The mechanism for reorientation of 60° rotated domains is unclear and might be template and/or crystal shape dependent, as a faster MoS_2 crystal shape evolution on the template with the larger 4º off-A axis cut angle and stable diamond-shaped configuration has led to some 60° rotated domains in the first monolayer. On the other hand, the MoS_2 monolayer lacks 60° rotated domains when deposited on 1 º off-A axis cut template, which is also reflected in the higher charge carriers 2PP mobility with mean value of 25 $cm^2 V^{-1} s^{-1}$. Hence, the mechanism responsible for the 60° rotated domains reorientation and its connection with the observed growth mechanism requires further

investigation. In addition, it is necessary to assess to which extent the discussed growth mechanism is dependent on the material and process conditions.

In the realm of nanoelectronics, the discovery of an alternative growth mechanism enabling the production of single crystalline MoS_2 monolayers with exceptional field-effect mobility promises further advancements in semiconductor technology.

Furthermore, the observed anisotropic growth phenomena on stepped surfaces can be exploited for a wider range of materials, enabling various applications in nanoelectronics, catalysis, nanotechnology and nanopatterning. In catalysis, the ability to manipulate crystal orientation and facet structure through substrate topography offers opportunities for designing highly efficient catalytic surfaces. Additionally, in nanotechnology, the observed anisotropic growth phenomena on stepped surfaces unlock the possibilities for engineering materials with tailored properties at the nanoscale, with applications spanning sensors, devices, and materials. Lastly, our findings can also have implications for nanopatterning, enabling precise control over material shapes and structures for the development of cutting-edge electronic and photonic devices. In essence, our research contributes to both fundamental understanding and transformative applications across various scientific and technological fields.

Methods

Sapphire templates. For bulk (0001) sapphire, the template is purposely cut from an ingot under an incident angle θ perpendicular to the [0001] axis and either towards the M-axis [1-100] and A-axis [11-20], with θ denoted as the off-axis cut angle. This angle determines the terrace width (W), according to the equation $W = \frac{H}{\tan(\theta)}$,[64] where H is the step height. The theoretical value for H is considered equal to 2.16 Å, as the distance between neighboring oxygen layers in the sapphire crystal structure. 2-inch single crystalline sapphire (0001, α-Al_2O_3) wafers purchased from the Roditi International Corporation are used in this study. The wafers are 330 μm thick and double side polished. There are three types of wafers, namely 1º off-A-axis cut sapphire, 4º off-A-axis cut sapphire, and on-axis cut sapphire. The sapphire wafers have a miscut angle of ± 0.1º.

Sapphire templates annealing. For the reconstruction study of sapphire surface topography, the wafers are annealed in EPSILON3200 reactor (ASM) in H_2 atmosphere for 1 h, total pressure in the chamber is 150 Torr.

MOCVD growth of MoS_2. MoS_2 monolayers are deposited using CVD with metal organic metal precursor and H_2S with relative concentrations [H_2S:$Mo(CO)_6$] = 32461. Higher vapor pressure of sulfur precursor compared to metal precursor was demonstrated to facilitate CVD of TMD leading to epitaxially deposited layer.[53,65] The deposition of MoS_2 takes place in adapted Polygon8200 cross flow reactor from ASM to enable MOCVD of MoS_2. The detailed description of the wafer's loading procedure is described elsewhere.[42] After loading the sapphire wafers to the reactor, the wafers are heated to the deposition temperature under high-purity N_2 atmosphere. There are two identical deposition processes used with the only difference in deposition temperature, one at 850 °C, the other one at 1000 °C. After reaching the deposition temperature in the reactor, 53 sccm H_2S carried by 20.12 slm N_2 and $1{,}63 \cdot 10^{-3}$

sccm $Mo(CO)_6$ carried by 6 sccm of Ar are introduced into the reactor chamber. Compressed gas cylinders provide high purity H_2S, N_2 and Ar gas. Vaporization of $Mo(CO)_6$ from the solid precursor (Air Liquide) takes place in a metallic canister at ~26 °C under ~900 mbar. The pressure in the deposition chamber is 75 Torr and the deposition temperature is constant. After the deposition, the cooling of the chamber is done in sulfur rich environment. The required time to deposit a closed monolayer is 180 min.

Atomic force microscopy (AFM). Dimension Icon from Bruker is used to characterize the morphology of sapphire surface and deposited MoS_2 crystals. The images are captured in PeakForce QNM mode using a silicon tip (HQ-NSC19/AlBS). Later, data is processed in Gwyddion software.

Rutherford Backscattering Spectrometry (RBS) is used to determine Mo:S ratio and the thickness of the deposited MoS_2 on sapphire. We used 1.523 MeV He+ ion beam and a scatter angle of 170º.

Plan-view Transmission Electron Microscopy (PV-TEM) is carried out on a Thermofisher Titan G2 operated at 200 kV on samples transferred to TEM grids with a tape assisted transfer method described elsewhere in more detail.[66] To reveal anti-phase or 60° rotated domains, a pair of complementary dark-field images are acquired with the smallest objective aperture (10 μm) positioned on opposite first order diffraction peaks. The two images are then overlaid with artificial colors red and green to enhance the contrast due to diffraction peak asymmetry in a monolayer of MoS_2. The detailed description is presented in.[42,67] The automated acquisition for DF-TEM montage is done on a Thermofisher Metrios operated at 200 kV.

In plane Grazing Incidence X-Ray Diffraction (GIXRD) measurements are done using a Malvern Panalytical X'PERT Pro diffractometer with PIXcel detector equipped with a Ni filter. In the setup copper is used to generate X-rays, while applying 40kV acceleration voltage and 45mA filament current to an X-ray tube. In between the X-ray tube and the sample stage, 0.7

mm divergence slit is placed. First, the setup is calibrated with sapphire $(11\bar{2}0)$ plane by performing the following steps: setting *2θ* value of 37.775°; placing X-ray tube, sample stage and X-rays detector within one plane; rotating the sample stage around the φ-axis and measuring X-rays diffraction. The maximum intensity is detected when sapphire $(11\bar{2}0)$ plane displays Bragg diffraction and further the orientation of the sapphire wafer is adjusted such that maximal diffraction occurs at φ= 0°. Next, *2θ is set* to 58.417°, φ to 0°, while varying the ω angle between -1 and 1°. The ω angle displaying maximal diffraction is used in subsequent measurements. The in-plane orientation of MoS_2 crystals is assessed by fixing *2θ,* ω and rotating the sample stage around the φ-axis from -95 to 95°, in steps of 0.04°.

Device Fabrication and Characterization. The detailed device fabrication process is described elsewhere.[42] The measurements are performed in N_2 ambient by a 300 mm semiautomatic probe station (PA300, Cascade) with Keithley B1500A at room temperature.

AUTHOR INFORMATION

Corresponding Author

Annelies Delabie

imec, Kapeldreef 75, Leuven, 3001, Belgium

Annelies.delabie@imec.be

Present Addresses

Yuanyuan Shi - ▲School of Microelectronics, University of Science and Technology of China (USTC), Jinzhai Road 96, Hefei, 230026, China

Author Contributions

The manuscript was written through contributions of all authors. All authors have given approval to the final version of the manuscript.

Funding Sources

Iryna Kandybka acknowledges funding from The Research Foundation – Flanders (FWO) for a Ph.D. fellowship strategic basic research (Project No. 1S60023N).

This work was done in the imec IIAP core CMOS programs and received funding from the European Union's Graphene Flagship grant agreement No 952792, 2D-EPL.

Data Availability Statement

The data that support the findings of this study are available from the corresponding author upon reasonable request.

Acknowledgements

We kindly acknowledge Johan Desmet and Johan Meersschaut for performing the RBS measurements.

We acknowledge Gerardo Martinez Alanis for developing the automation recipe for acquisition of images in a grid pattern with a predefined overlap for DF-TEM montaging.

Supporting Information Available

Additional information about step-flow growth mode, flattening of AFM images, AFM of MoS_2 on the on-axis cut sapphire, determination of the temperature of sapphire surface reconstruction, AFM of the MoS_2 crystals grown at 850 ºC, TEM images of the MoS_2 monolayers, channel length dependent 2PP mobility, TLM mobility of charge carriers, optical characterization of the closed MoS_2 monolayers (Raman, PL).

REFERENCES

(1) Akinwande, D.; Huyghebaert, C.; Wang, C. H.; Serna, M. I.; Goossens, S.; Li, L. J.; Wong, H. S. P.; Koppens, F. H. L. Graphene and Two-Dimensional Materials for Silicon Technology. *Nature* **2019**, *573*, 507–518. https://doi.org/10.1038/s41586-019-1573-9.

(2) Naikoo, G. A.; Arshad, F.; Almas, M.; Hassan, I. U.; Pedram, M. Z.; Aljabali, A. A. A.; Mishra, V.; Serrano-Aroca, Á.; Birkett, M.; Charbe, N. B.; Goyal, R.; Negi, P.; El-Tanani, M.; Tambuwala, M. M. 2D Materials, Synthesis, Characterization and Toxicity: A Critical Review. *Chem Biol Interact* **2022**, *365*, 110081. https://doi.org/10.1016/J.CBI.2022.110081.

(3) Shanmugam, V.; Mensah, R. A.; Babu, K.; Gawusu, S.; Chanda, A.; Tu, Y.; Neisiany, R. E.; Försth, M.; Sas, G.; Das, O.; Shanmugam, V.; Mensah, R. A.; Försth, M.; Sas, G.; Das, O.; Babu, K.; Gawusu, S.; Tu, Y.; Neisiany, R. E. A Review of the Synthesis, Properties, and Applications of 2D Materials. *Particle & Particle Systems Characterization* **2022**, *39*, 2200031. https://doi.org/10.1002/PPSC.202200031.

(4) Qi, Y.; Sadi, M. A.; Hu, D.; Zheng, M.; Wu, Z.; Jiang, Y.; Chen, Y. P. Recent Progress in Strain Engineering on Van Der Waals 2D Materials: Tunable Electrical, Electrochemical, Magnetic, and Optical Properties. *Advanced Materials* **2023**, *35*, 2205714. https://doi.org/10.1002/ADMA.202205714.

(5) Lin, Y. C.; Torsi, R.; Younas, R.; Hinkle, C. L.; Rigosi, A. F.; Hill, H. M.; Zhang, K.; Huang, S.; Shuck, C. E.; Chen, C.; Lin, Y. H.; Maldonado-Lopez, D.; Mendoza-Cortes, J. L.; Ferrier, J.; Kar, S.; Nayir, N.; Rajabpour, S.; van Duin, A. C. T.; Liu, X.; Jariwala, D. *et al*. Recent Advances in 2D Material Theory, Synthesis, Properties, and Applications. *ACS Nano* **2023**, *17*, 9694–9747. https://doi.org/10.1021/ACSNANO.2C12759.

(6) Cai, Z.; Liu, B.; Zou, X.; Cheng, H. M. Chemical Vapor Deposition Growth and Applications of Two-Dimensional Materials and Their Heterostructures. *Chem Rev* **2018**, *118*, 6091–6133. https://doi.org/https://doi.org/10.1021/acs.chemrev.7b00536.

(7) Glavin, N. R.; Rao, R.; Varshney, V.; Bianco, E.; Apte, A.; Roy, A.; Ringe, E.; Ajayan, P. M. Emerging Applications of Elemental 2D Materials. *Advanced Materials* **2020**, *32*, 1904302. https://doi.org/10.1002/ADMA.201904302.

(8) Zhang, R.; Jiang, J.; Wu, W. Wearable Chemical Sensors Based on 2D Materials for Healthcare Applications. *Nanoscale* **2023**, *15*, 3079–3105. https://doi.org/10.1039/D2NR05447G.

(9) Elbanna, A.; Jiang, H.; Fu, Q.; Zhu, J. F.; Liu, Y.; Zhao, M.; Liu, D.; Lai, S.; Chua, X. W.; Pan, J.; Shen, Z. X.; Wu, L.; Liu, Z.; Qiu, C. W.; Teng, J. 2D Material Infrared Photonics and Plasmonics. *ACS Nano* **2023**, *17*, 4134–4179. https://doi.org/10.1021/ACSNANO.2C10705.

(10) Hu, Z.; Wu, Z.; Han, C.; He, J.; Ni, Z.; Chen, W. Two-Dimensional Transition Metal Dichalcogenides: Interface and Defect Engineering. *Chemical Society Reviews* **2018**, 47, 3100–3128. https://doi.org/10.1039/c8cs00024g.

(11) Shen, Y.; Dong, Z.; Sun, Y.; Guo, H.; Wu, F.; Li, X.; Tang, J.; Liu, J.; Wu, X.; Tian, H.; Ren, T.-L.; Shen, Y.; Wu, F.; Tian, H.; Ren, T.-L.; Dong, Z.; Sun, Y.; Li, X.; Wu, X.; Guo, H. *et al*. The Trend of 2D Transistors toward Integrated Circuits: Scaling Down and New Mechanisms. *Advanced Materials* **2022**, *34*, 2201916. https://doi.org/10.1002/ADMA.202201916.

(12) McDonnell, S. J.; Wallace, R. M. Atomically-Thin Layered Films for Device Applications Based upon 2D TMDC Materials. *Thin Solid Films* **2016**, *616*, 482–501. https://doi.org/10.1016/J.TSF.2016.08.068.

(13) Cheng, Z.; Yu, Y.; Singh, S.; Price, K.; Noyce, S. G.; Lin, Y. C.; Cao, L.; Franklin, A. D. Immunity to Contact Scaling in MoS2 Transistors Using in Situ Edge Contacts. *Nano Lett* **2019**, *19*, 5077–5085. https://doi.org/10.1021/acs.nanolett.9b01355.

(14) Radisavljevic, B.; Kis, A. Mobility Engineering and a Metal–Insulator Transition in Monolayer MoS2. *Nature Materials* **2013**, *12*, 815–820. https://doi.org/10.1038/nmat3687.

(15) Zavabeti, A.; Jannat, A.; Zhong, L.; Haidry, A. A.; Yao, Z.; Ou, J. Z. Two-Dimensional Materials in Large-Areas: Synthesis, Properties and Applications. *Nano-Micro Letters* **2020**, 12, 66. https://doi.org/10.1007/s40820-020-0402-x.

(16) Bian, R.; Li, C.; Liu, Q.; Cao, G.; Fu, Q.; Meng, P.; Zhou, J.; Liu, F.; Liu, Z. Recent Progress in the Synthesis of Novel Two-Dimensional van Der Waals Materials. *Natl Sci Rev* **2022**, *9*, nwab164. https://doi.org/10.1093/NSR/NWAB164.

(17) Kim, S.-Y.; Kwak, J.; Ciobanu, C. V; Kwon, S.-Y.; Kim, S.; Kwak, J.; Kwon, S.; Ciobanu, C. V. Recent Developments in Controlled Vapor-Phase Growth of 2D Group 6 Transition Metal Dichalcogenides. *Advanced Materials* **2019**, *31*, 1804939. https://doi.org/10.1002/ADMA.201804939.

(18) Zhang, Y.; Yao, Y.; Sendeku, M. G.; Yin, L.; Zhan, X.; Wang, F.; Wang, Z.; He, J. Recent Progress in CVD Growth of 2D Transition Metal Dichalcogenides and Related Heterostructures. *Advanced Materials* **2019**, *31*, 1901694. https://doi.org/10.1002/ADMA.201901694.

(19) Rai, A.; Movva, H. C. P.; Roy, A.; Taneja, D.; Chowdhury, S.; Banerjee, S. K. Progress in Contact, Doping and Mobility Engineering of MoS_2: An Atomically Thin 2D Semiconductor. *Crystals* **2018**, *8*, 316. https://doi.org/10.3390/cryst8080316.

(20) Najmaei, S.; Yuan, J.; Zhang, J.; Ajayan, P.; Lou, J. Synthesis and Defect Investigation of Two-Dimensional Molybdenum Disulfide Atomic Layers. *Acc Chem Res* **2015**, *48*, 31–40. https://doi.org/10.1021/ar500291j.

(21) Koma, A. Heteroepitaxy Between Lattice Mismatched Materials with Van Der Waals Interactions. *MRS Proceedings* **1990**, *198*, 105–110. https://doi.org/10.1557/proc-198-105.

(22) Koma, A.; Saiki, K.; Sato, Y. Heteroepitaxy of a Two-Dimensional Material on a Three-Dimensional Material. *Appl Surf Sci* **1990**, *41–42*, 451–456. https://doi.org/10.1016/0169-4332(89)90102-5.

(23) Choudhury, T. H.; Zhang, X.; Al Balushi, Z. Y.; Chubarov, M.; Redwing, J. M. Epitaxial Growth of Two-Dimensional Layered Transition Metal Dichalcogenides. *Annu Rev Mater Res* **2020**, *50*, 155–177. https://doi.org/10.1146/annurev-matsci-090519-113456.

(24) Dumcenco, D.; Ovchinnikov, D.; Marinov, K.; Lazić, P.; Gibertini, M.; Marzari, N.; Sanchez, O. L.; Kung, Y. C.; Krasnozhon, D.; Chen, M. W.; Bertolazzi, S.; Gillet, P.;

Fontcuberta I Morral, A.; Radenovic, A.; Kis, A. Large-Area Epitaxial Monolayer MoS_2. *ACS Nano* **2015**, *9*, 4611–4620. https://doi.org/10.1021/acsnano.5b01281.

(25) Ji, Q.; Kan, M.; Zhang, Y.; Guo, Y.; Ma, D.; Shi, J.; Sun, Q.; Chen, Q.; Zhang, Y.; Liu, Z. Unravelling Orientation Distribution and Merging Behavior of Monolayer MoS_2 Domains on Sapphire. *Nano Lett* **2015**, *15*, 198–205. https://doi.org/10.1021/NL503373X.

(26) Van Der Zande, A. M.; Huang, P. Y.; Chenet, D. A.; Berkelbach, T. C.; You, Y.; Lee, G. H.; Heinz, T. F.; Reichman, D. R.; Muller, D. A.; Hone, J. C. Grains and Grain Boundaries in Highly Crystalline Monolayer Molybdenum Disulphide. *Nature Materials* **2013**, *12*, 554–561. https://doi.org/10.1038/nmat3633.

(27) Du, L.; Yu, H.; Xie, L.; Wu, S.; Wang, S.; Lu, X.; Liao, M.; Meng, J.; Zhao, J.; Zhang, J.; Zhu, J.; Chen, P.; Wang, G.; Yang, R.; Shi, D.; Zhang, G. The Effect of Twin Grain Boundary Tuned by Temperature on the Electrical Transport Properties of Monolayer MoS_2. *Crystals* **2016**, *6*, 115. https://doi.org/10.3390/CRYST6090115.

(28) Zhang, Z.; Yang, X.; Liu, K.; Wang, R. Epitaxy of 2D Materials toward Single Crystals. *Advanced Science* **2022**, *9*, 2105201. https://doi.org/10.1002/advs.202105201.

(29) Yang, P.; Wang, D.; Zhao, X.; Quan, W.; Jiang, Q.; Li, X.; Tang, B.; Hu, J.; Zhu, L.; Pan, S.; Shi, Y.; Huan, Y.; Cui, F.; Qiao, S.; Chen, Q.; Liu, Z.; Zou, X.; Zhang, Y. Epitaxial Growth of Inch-Scale Single-Crystal Transition Metal Dichalcogenides through the Patching of Unidirectionally Orientated Ribbons. *Nature Communications* **2022**, *13*, 3238. https://doi.org/10.1038/s41467-022-30900-9.

(30) Zhu, H.; Nayir, N.; Choudhury, T. H.; Bansal, A.; Huet, B.; Zhang, K.; Puretzky, A. A.; Bachu, S.; York, K.; Mc Knight, T. V.; Trainor, N.; Oberoi, A.; Wang, K.; Das, S.; Makin, R. A.; Durbin, S. M.; Huang, S.; Alem, N.; Crespi, V. H.; van Duin, A. C. T. *et al*. Step Engineering for Nucleation and Domain Orientation Control in WSe_2 Epitaxy on C-Plane Sapphire. *Nature Nanotechnology* **2023**, 18, 1295–1302. https://doi.org/10.1038/s41565-023-01456-6.

(31) Li, T.; Guo, W.; Ma, L.; Li, W.; Yu, Z.; Han, Z.; Gao, S.; Liu, L.; Fan, D.; Wang, Z.; Yang, Y.; Lin, W.; Luo, Z.; Chen, X.; Dai, N.; Tu, X.; Pan, D.; Yao, Y.; Wang, P.; Nie, Y. *et al*. Epitaxial Growth of Wafer-Scale Molybdenum Disulfide Semiconductor Single Crystals on Sapphire. *Nature Nanotechnology* **2021**, *16*, 1201–1207. https://doi.org/10.1038/s41565-021-00963-8.

(32) Wang, J.; Xu, X.; Cheng, T.; Gu, L.; Qiao, R.; Liang, Z.; Ding, D.; Hong, H.; Zheng, P.; Zhang, Z.; Zhang, Z.; Zhang, S.; Cui, G.; Chang, C.; Huang, C.; Qi, J.; Liang, J.; Liu, C.; Zuo, Y.; Xue, G. *et al*. Dual-Coupling-Guided Epitaxial Growth of Wafer-Scale Single-Crystal WS_2 Monolayer on Vicinal a-Plane Sapphire. *Nature Nanotechnology* **2021**, *17*, 33–38. https://doi.org/10.1038/s41565-021-01004-0.

(33) Chubarov, M.; Choudhury, T. H.; Hickey, D. R.; Bachu, S.; Zhang, T.; Sebastian, A.; Bansal, A.; Zhu, H.; Trainor, N.; Das, S.; Terrones, M.; Alem, N.; Redwing, J. M. Wafer-Scale Epitaxial Growth of Unidirectional WS_2 Monolayers on Sapphire. *ACS Nano* **2021**, *15*, 2532–2541. https://doi.org/10.1021/ACSNANO.0C06750.

(34) Chen, L.; Liu, B.; Ge, M.; Ma, Y.; Abbas, A. N.; Zhou, C. Step-Edge-Guided Nucleation and Growth of Aligned WSe_2 on Sapphire via a Layer-over-Layer Growth Mode. *ACS Nano* **2015**, *9*, 8368–8375. https://doi.org/10.1021/ACSNANO.5B03043.

(35) Burton W. K.; Cabrea N.; Frank F. C. The Growth of Crystals and the Equilibrium Structure of Their Surfaces. *Philosophical Transactions of the Royal Society of London. Series A, Mathematical and Physical Sciences* **1951**, *243*, 299–358. https://doi.org/10.1098/rsta.1951.0006.

(36) Fu, J.-H.; Min, J.; Chang, C.-K.; Tseng, C.-C.; Wang, Q.; Sugisaki, H.; Li, C.; Chang, Y.-M.; Alnami, I.; Syong, W.-R.; Lin, C.; Fang, F.; Zhao, L.; Lo, T.-H.; Lai, C.-S.; Chiu, W.-S.; Jian, Z.-S.; Chang, W.-H.; Lu, Y.-J.; Shih, K. *et al*. Oriented Lateral Growth of Two-Dimensional Materials on c-Plane Sapphire. *Nature Nanotechnology* **2023**, 18, 1289–1294. https://doi.org/10.1038/s41565-023-01445-9.

(37) Van Pham, L.; Kurnosikov, O.; Cousty, J. Evolution of Steps on Vicinal (0001) Surfaces of α-Alumina. *Surface Science* **1998**, *411*, 263–271. https://doi.org/10.1016/s0039-6028(98)00329-x.

(38) Butashin, A. V.; Vlasov, V. P.; Kanevskii, V. M.; Muslimov, A. E.; Fedorov, V. A. Specific Features of the Formation of Terrace-Step Nanostructures on the (0001) Surface of Sapphire Crystals. *Crystallography Reports* **2012**, *57*, 824–830. https://doi.org/10.1134/S1063774512060193.

(39) Cuccureddu, F.; Murphy, S.; Shvets, I. V.; Porcu, M.; Zandbergen, H. W.; Sidorov, N. S.; Bozhko, S. I. Surface Morphology of C-Plane Sapphire (α-Alumina) Produced by High Temperature Anneal. *Surface Science* **2010**, *604*, 1294–1299. https://doi.org/10.1016/j.susc.2010.04.017.

(40) Shiratsuchi, Y.; Yamamoto, M.; Kamada, Y. Surface Structure of Self-Organized Sapphire (0001) Substrates with Various Inclined Angles. *Japanese Journal of Applied Physics, Part 1: Regular Papers and Short Notes and Review Papers* **2002**, *41*, 5719–5725. https://doi.org/10.1143/jjap.41.5719.

(41) Zheng, P.; Wei, W.; Liang, Z.; Qin, B.; Tian, J.; Wang, J.; Qiao, R.; Ren, Y.; Chen, J.; Huang, C.; Zhou, X.; Zhang, G.; Tang, Z.; Yu, D.; Ding, F.; Liu, K.; Xu, X. Universal Epitaxy of Non-Centrosymmetric Two-Dimensional Single-Crystal Metal Dichalcogenides. *Nature Communications* **2023**, *14*, 592. https://doi.org/10.1038/s41467-023-36286-6.

(42) Shi, Y.; Groven, B.; Serron, J.; Wu, X.; Nalin Mehta, A.; Minj, A.; Sergeant, S.; Han, H.; Asselberghs, I.; Lin, D.; Brems, S.; Huyghebaert, C.; Morin, P.; Radu, I.; Caymax, M. Engineering Wafer-Scale Epitaxial Two-Dimensional Materials through Sapphire Template Screening for Advanced High-Performance Nanoelectronics. *ACS Nano* **2021**, *15*, 9482–9494. https://doi.org/10.1021/ACSNANO.0C07761.

(43) Zhang, J.; Wang, F.; Shenoy, V. B.; Tang, M.; Lou, J. Towards Controlled Synthesis of 2D Crystals by Chemical Vapor Deposition (CVD). *Materials Today* **2020**, *40*, 132–139. https://doi.org/10.1016/J.MATTOD.2020.06.012.

(44) Byskov, L. S.; Nørskov, J. K.; Clausen, B. S.; Topsøe, H. Edge Termination of MoS_2 and CoMoS Catalyst Particles. *Catalysis Letters* **2000**, *64*, 95–99. https://doi.org/10.1023/A:1019063709813.

(45) Zhang, Z.; Lagally, M. G. Atomistic Processes in the Early Stages of Thin-Film Growth. *Science* **1997**, 276, 377–383. https://doi.org/10.1126/science.276.5311.377.

(46) Wang, S. C.; Ehrlich, G. Atom Incorporation at Surface Clusters: An Atomic View. *Phys Rev Lett* **1991**, *67*, 2509. https://doi.org/10.1103/PhysRevLett.67.2509.

(47) Schwoebel, R. L. Step Motion on Crystal Surfaces. II. *J Appl Phys* **1969**, *40*, 614–618. https://doi.org/10.1063/1.1657442.

(48) Caymax, M.; Kazzi, S. El; Huyghebaert, C. MOCVD Growth of 2D WS_2 on SiO_2: Nucleation Mechanism and Kinetics. *Extended Abstracts of the 2019 International Conference on Solid State Devices and Materials, Nagoya* **2019**, 159–160. https://doi.org/10.1002/aic.690450217.

(49) Dong, J.; Ding, D.; Jin, C.; Liu, Y.; Ding, F. Edge Reconstruction-Dependent Growth Kinetics of MoS_2. *ACS Nano* **2023**, *17*, 127–136. https://doi.org/10.1021/ACSNANO.2C05397.

(50) Sebastian, A.; Pendurthi, R.; Choudhury, T. H.; Redwing, J. M.; Das, S. Benchmarking Monolayer MoS_2 and WS_2 Field-Effect Transistors. *Nature Communications* **2021**, *12*, 693. https://doi.org/10.1038/s41467-020-20732-w.

(51) Zhang, X.; Choudhury, T. H.; Chubarov, M.; Xiang, Y.; Jariwala, B.; Zhang, F.; Alem, N.; Wang, G. C.; Robinson, J. A.; Redwing, J. M. Diffusion-Controlled Epitaxy of Large Area Coalesced WSe_2 Monolayers on Sapphire. *Nano Lett* **2018**, *18*, 1049–1056. https://doi.org/10.1021/acs.nanolett.7b04521.

(52) Yu, H.; Liao, M.; Zhao, W.; Liu, G.; Zhou, X. J.; Wei, Z.; Xu, X.; Liu, K.; Hu, Z.; Deng, K.; Zhou, S.; Shi, J. A.; Gu, L.; Shen, C.; Zhang, T.; Du, L.; Xie, L.; Zhu, J.; Chen, W.; Yang, R. *et al*. Wafer-Scale Growth and Transfer of Highly-Oriented Monolayer MoS_2 Continuous Films. *ACS Nano* **2017**, *11*, 12001–12007. https://doi.org/10.1021/ACSNANO.7B03819.

(53) Aljarb, A.; Cao, Z.; Tang, H. L.; Huang, J. K.; Li, M.; Hu, W.; Cavallo, L.; Li, L. J. Substrate Lattice-Guided Seed Formation Controls the Orientation of 2D Transition-Metal Dichalcogenides. *ACS Nano* **2017**, *11*, 9215–9222. https://doi.org/10.1021/ACSNANO.7B04323.

(54) Rogge, P. C.; Thürmer, K.; Foster, M. E.; McCarty, K. F.; Dubon, O. D.; Bartelt, N. C. Real-Time Observation of Epitaxial Graphene Domain Reorientation. *Nature Communications* **2015**, *6*, 6880. https://doi.org/10.1038/ncomms7880.

(55) Lin, Y. C.; Dumcenco, D. O.; Huang, Y. S.; Suenaga, K. Atomic Mechanism of the Semiconducting-to-Metallic Phase Transition in Single-Layered MoS_2. *Nature Nanotechnology* **2014**, *9*, 391–396. https://doi.org/10.1038/nnano.2014.64.

(56) Leonhardt, A.; Chiappe, D.; Asselberghs, I.; Huyghebaert, C.; Radu, I.; De Gendt, S. Improving MOCVD MoS_2 Electrical Performance: Impact of Minimized Water and Air

Exposure Conditions. *IEEE Electron Device Letters* **2017**, *38*, 1606–1609. https://doi.org/10.1109/LED.2017.2752424.

(57) Cun, H.; Macha, M.; Kim, H. K.; Liu, K.; Zhao, Y.; LaGrange, T.; Kis, A.; Radenovic, A. Wafer-Scale MOCVD Growth of Monolayer MoS_2 on Sapphire and SiO_2. *Nano Res* **2019**, *12*, 2646–2652. https://doi.org/10.1007/s12274-019-2502-9.

(58) Park, J. H.; Lu, A. Y.; Shen, P. C.; Shin, B. G.; Wang, H.; Mao, N.; Xu, R.; Jung, S. J.; Ham, D.; Kern, K.; Han, Y.; Kong, J. Synthesis of High-Performance Monolayer Molybdenum Disulfide at Low Temperature. *Small Methods* **2021**, *5*, 2000720. https://doi.org/10.1002/SMTD.202000720.

(59) Kang, K.; Xie, S.; Huang, L.; Han, Y.; Huang, P. Y.; Mak, K. F.; Kim, C. J.; Muller, D.; Park, J. High-Mobility Three-Atom-Thick Semiconducting Films with Wafer-Scale Homogeneity. *Nature* **2015**, *520*, 656–660. https://doi.org/10.1038/nature14417.

(60) Kim, T. S.; Dhakal, K. P.; Park, E.; Noh, G.; Chai, H.-J.; Kim, Y.; Oh, S.; Kang, M.; Park, J.; Kim, J.; Kim, S.; Jeong, Y.; Bang, S.; Kwak, J. Y.; Kim, J.; Kang, K.; Kim, T. S.; Noh, G.; Chai, H.-J.; Oh, S. *et al*. Gas-Phase Alkali Metal-Assisted MOCVD Growth of 2D Transition Metal Dichalcogenides for Large-Scale Precise Nucleation Control. *Small* **2022**, *18*, 2106368. https://doi.org/10.1002/SMLL.202106368.

(61) Carlsson, J. O. Selective Vapor-Phase Deposition on Patterned Substrates. *Critical Reviews in Solid State and Materials Sciences* **1990**, *16*, 161–212. https://doi.org/10.1080/10408439008244628.

(62) Parsons, G. N.; Clark, R. D. Area-Selective Deposition: Fundamentals, Applications, and Future Outlook. *Chemistry of Materials* **2020**, *32*, 4920–4953. https://doi.org/10.1021/ACS.CHEMMATER.0C00722.

(63) Cao, K.; Cai, J.; Chen, R. Inherently Selective Atomic Layer Deposition and Applications. *Chemistry of Materials* **2020**, *32*, 2195–2207. https://doi.org/10.1021/ACS.CHEMMATER.9B04647.

(64) Hayashi, Y.; Banal, R. G.; Funato, M.; Kawakami, Y. Heteroepitaxy between Wurtzite and Corundum Materials. *J Appl Phys* **2013**, *113*, 183523. https://doi.org/10.1063/1.4804328.

(65) Xue, H.; Wu, G.; Zhao, B.; Wang, D.; Wu, X.; Hu, Z. High-Temperature in Situ Investigation of Chemical Vapor Deposition to Reveal Growth Mechanisms of Monolayer Molybdenum Disulfide. *ACS Appl Electron Mater* **2020**, *2*, 1925–1933. https://doi.org/10.1021/ACSAELM.0C00231.

(66) Nalin Mehta, A.; Mo, J.; Pourtois, G.; Dabral, A.; Groven, B.; Bender, H.; Favia, P.; Caymax, M.; Vandervorst, W. Grain-Boundary-Induced Strain and Distortion in Epitaxial Bilayer MoS_2 Lattice. *The Journal of Physical Chemistry C* **2020**, *124*, 6472–6478. https://doi.org/10.1021/ACS.JPCC.0C01468.

(67) Nalin Mehta, A.; Gauquelin, N.; Nord, M.; Orekhov, A.; Bender, H.; Cerbu, D.; Verbeeck, J.; Vandervorst, W. Unravelling Stacking Order in Epitaxial Bilayer MX2 Using 4D-STEM with Unsupervised Learning. *Nanotechnology* **2020**, *31*, 445702. https://doi.org/10.1088/1361-6528/ABA5B6.

For Table of Contents Only